Int. J. Solids Structures Vol. 23, No. 3, pp. 413–437, 1987
Printed in Great Britain.

0020-7683/87 $3.00+.00

A FINITE ELEMENT ANALYSIS OF THE INCLUSION PROBLEM FOR POWER LAW VISCOUS MATERIALS

P. GILORMINI and Y. GERMAIN
Centre de Mise en Forme des Matériaux, Ecole des Mines de Paris, GRECO CNRS Grandes Déformations et Endommagement, UA 852, Sophia-Antipolis, 06560 Valbonne, France

(*Received* 21 *June* 1985; *in revised form* 7 *April* 1986)

Abstract—A finite element analysis is developed for the study of the inclusion problem in the case of power law viscous materials, and a method for the derivation of inclusion–matrix interface tractions is included. A close study of the mesh is detailed, which grounds on the analytical solution for a linearly viscous matrix. After preliminary tests are performed, the finite element program is applied to many cases of cylindrical or spheroidal inclusions with various hardness and aspect ratios and rate sensitivities. Results concerning as well the average strain rate and its distribution in the inclusion as the maximal tensile traction normal to the interface are presented and discussed.

1. INTRODUCTION

The determination of stresses and strains induced by a change in form or an inhomogeneity of composition in a finite region of a deformable medium has been a wide field of investigation for many authors since the dawn of continuum mechanics. Several different situations are included in the general inclusion problem.

(1) A finite region (referred to as "the inclusion") in a deformable medium changes in shape or size (e.g. thermal expansion). This is often called "the inclusion problem" and includes two branches according to whether the inclusion has the same behaviour as the surrounding matrix or not. This covers, for instance, the stresses and strains around dislocations or martensitic transformation in steels.

(2) A deformable medium is loaded which contains an inhomogeneity of composition (an "inclusion" in the metallurgist's terminology) or even a cavity. This is often termed as "the inhomogeneity problem" and covers, for instance, the study of damage initiation in metals and the growth of holes in creep or ductile fracture. If the cavity is merely a particular inhomogeneity for elastic materials (Young's modulus falling to zero in the inclusion) it is not the case for incompressible plastic materials because of the non-zero hydrostatic pressure within the inclusion which stems from the difference between an empty cavity and a hole filled with an inviscid fluid.

These problems are closely related and have been studied for various behaviours (elasticity, viscoelasticity, elastoplasticity, plasticity, viscoplasticity), geometrical conditions (inclusions of various shapes, finite or infinite matrix) and loadings (uniform, polynomial or periodic deformation of the inclusion or loading of the matrix). In the following sections of this paper attention is focused on the inhomogeneity problem which is called "the inclusion problem" henceforward.

The main contribution to the inclusion problem in elasticity is due to Eshelby[1] for the case of an ellipsoidal inclusion embedded in an unbounded matrix uniformly loaded at infinity. This work was extended by many authors including Walpole[2] for anisotropic elasticity, Kunin and Sosnina[3] for polynomial loading at infinity, Johnson *et al.*[4] for arbitrarily shaped inclusions, Theocaris and Ioakimidis[5] for finite matrix. Analytical solutions can be derived in the case of elasticity or viscoelasticity (e.g. Hashin[6], Laws and McLaughlin[7]), which are often obtained under highly implicit forms, but the study of non-linear behaviours requires numerical solutions. Variational semi-analytical approaches have been used for the growth of holes (Rice and Tracey[8], Gurson[9], Budiansky *et al.*[10]) or inclusion deformation (Gilormini and Montheillet[11]) for rigid–

plastic or viscoplastic materials. The finite difference method has been used by Tuba[12] in the plane strain case of a cylindrical rigid inclusion (see also Orr and Brown[13]) or a cylindrical hole in an elastic–plastic matrix with linear strain hardening, and Huang[14] for power law strain hardening or power law viscous matrix. The finite element method has been more widely used: Marcal and King[15], Zienkiewicz *et al.*[16] and Eimermacher *et al.*[17] have studied the case of a central hole in an elastic–plastic strain hardening flat plate in tension, the plain strain case of cylindrical voids was investigated by Needleman[18], Nemat-Nasser and Taya[19] for strain hardening materials and by Andersson[20] for the elastic–perfectly plastic behaviour. The axisymmetric case of a spherical rigid or elastic inclusion in an elastic–plastic matrix with power law hardening was studied by Thomson and Hancock[21] using the MARC finite element program. A finite element analysis was also developed by Burke and Nix[22] for the case of a doubly periodic square array of cylindrical voids in a power law viscous matrix.

The problem of deformable inclusions in the case of power law viscous materials has received very little attention (e.g. see Refs [11, 23]) as far as the authors know. The present paper, where no strain hardening is considered, aims at contributing to this field which concerns the change in shape of non-metallic inclusions and damage initiation due to stress concentrations in steels during creep, metal-working in the hot range and superplastic materials. A finite element analysis is proposed which includes an original calculation of the radial stresses at the inclusion–matrix interface. Deformable elliptic cylindrical or spheroidal inclusions are considered in plane strain and axisymmetric deformation, respectively. A close study of the mesh is detailed which is grounded on the exact analytical solution for linearly viscous materials. Original results concerning the strain rate inhomogeneity in the inclusion and the maximum stress normal to the interface are finally presented and discussed.

2. VARIATIONAL FORMULATION

The minimum principle for velocities developed by Hill[24] in the case of incompressible power law viscous materials states that the velocities minimize the functional

$$f = \int_{V \cup \Omega} \frac{\sigma}{m+1} \dot{\bar{\varepsilon}}^{m+1} \, dV \tag{1}$$

if the velocity is imposed on the whole outer surface of the material and provided the body and inertial forces are negligible. In the above equation V and Ω are the finite volumes of the matrix and the inclusion, respectively. The velocities v_i must fulfil the prescribed boundary conditions on the outer surface of V, be continuous in $V \cup \Omega$, and satisfy the incompressibility equation

$$v_{i,i} = 0 \tag{2}$$

$\dot{\bar{\varepsilon}}$ is the effective strain rate

$$\dot{\bar{\varepsilon}} = \left(\frac{2}{3} \dot{\varepsilon}_{ij} \dot{\varepsilon}_{ij} \right)^{1/2} \tag{3}$$

where

$$\dot{\varepsilon}_{ij} = \frac{1}{2}(v_{i,j} + v_{j,i}) \tag{4}$$

σ and m take the values σ_M and m_M in the matrix and σ_I and m_I in the inclusion. The flow rule is

$$s_{ij} = \frac{2}{3}\sigma\dot{\bar{\varepsilon}}^{m-1}\dot{\varepsilon}_{ij} \tag{5}$$

where s_{ij} is the deviatoric part of the stress tensor, σ is a reference flow stress for $\dot{\bar{\varepsilon}} = 1\,s^{-1}$ and m is the rate hardening exponent ranging from 0 (rigid–plastic behaviour for which eqn (5) applies if the yield condition is fulfilled only) to 1 (linearly viscous materials).

In order to simplify the finite element analysis, the incompressibility condition eqn (2) was not imposed on the velocity field and the following functional was consequently used

$$g = f + \frac{1}{2}\rho\int_{V\cup\Omega}(\dot{\varepsilon}_{ii})^2\,dV \tag{6}$$

since it has been established[25] that the minimization of g gives the same solution as the minimization of f when ρ tends to infinity (exterior penalty method). For numerical reasons ρ must be taken equal to a finite (although great) value which can be interpreted as an expansion coefficient in the case of a compressible material and immediately leads to the following expression for the associated hydrostatic pressure

$$p = -\rho\dot{\varepsilon}_{ii}. \tag{7}$$

The value of ρ was chosen practically so as to obtain a very good approximation to eqn (2) while p remained finite. This procedure gave very satisfactory values of the velocity and hydrostatic pressure fields for incompressible materials, as shown below by the comparison with the exact analytical solution in the case of a linearly viscous behaviour.

3. FINITE ELEMENT ANALYSIS

The velocity field is described in an approximate manner according to the finite element method of analysis by the relationship

$$\mathbf{v} = \mathbf{N}\mathbf{a} \tag{8}$$

where $\mathbf{a}$ is the vector of nodal point velocities and $\mathbf{N}$ is the matrix of interpolating functions which are associated with each of the nodes. A classical four-node quadrilateral isoparametric element is used here[26], the velocity components within each element are approximated consequently by polynomials including terms in x, y, xy and constants, where x and y are rectangular Cartesian coordinates in the plane strain case and denote the usual r- and z-coordinates in the meridional section in the case of axial symmetry around the y-axis.

The associated strain rate tensor can be written as a vector $\dot{\boldsymbol{\varepsilon}}$ defined as

$$\dot{\boldsymbol{\varepsilon}} = \begin{bmatrix} \dot{\varepsilon}_{xx} \\ \dot{\varepsilon}_{yy} \\ 2\dot{\varepsilon}_{xy} \end{bmatrix} \quad \text{and} \quad \begin{bmatrix} \dot{\varepsilon}_{xx} \\ \dot{\varepsilon}_{yy} \\ \dot{\varepsilon}_{\theta\theta} \\ 2\dot{\varepsilon}_{xy} \end{bmatrix} \tag{9}$$

in the plane strain and axisymmetric cases, respectively, where θ is the angular coordinate around the y-axis in the latter case. This leads to the following relationship between $\dot{\boldsymbol{\varepsilon}}$ and $\mathbf{a}$

$$\dot{\boldsymbol{\varepsilon}} = \mathbf{N}'\mathbf{a} \tag{10}$$

with $\mathbf{N}' = \mathbf{LN}$

$$\mathbf{L} = \begin{bmatrix} \frac{\partial}{\partial x} & 0 \\ 0 & \frac{\partial}{\partial y} \\ \frac{\partial}{\partial y} & \frac{\partial}{\partial x} \end{bmatrix} \quad \text{and} \quad \begin{bmatrix} \frac{\partial}{\partial x} & 0 \\ 0 & \frac{\partial}{\partial y} \\ \frac{1}{x} & 0 \\ \frac{\partial}{\partial y} & \frac{\partial}{\partial x} \end{bmatrix} \tag{11}$$

the plane strain and axisymmetric cases, respectively. The functional g defined above can be written after finite element discretization as

$$g = \sum_{i=1}^{N_e} \int_{V_i} \left\{ \frac{\sigma}{m+1} ({}^{\mathrm{T}}\mathbf{a}\,{}^{\mathrm{T}}\mathbf{N}'\mathbf{M}\,\mathbf{N}'\mathbf{a})^{(m+1)/2} + \frac{1}{2}\rho({}^{\mathrm{T}}\mathbf{M}'\mathbf{N}'\mathbf{a})^2 \right\} \mathrm{d}V \tag{12}$$

where N_e is the total number of elements, V_i is the ith element volume

$$\mathbf{M} = \frac{1}{3}\begin{bmatrix} 2 & 0 & 0 \\ 0 & 2 & 0 \\ 0 & 0 & 1 \end{bmatrix} \quad \text{and} \quad \frac{1}{3}\begin{bmatrix} 2 & 0 & 0 & 0 \\ 0 & 2 & 0 & 0 \\ 0 & 0 & 2 & 0 \\ 0 & 0 & 0 & 1 \end{bmatrix} \tag{13}$$

$$ {}^{\mathrm{T}}\mathbf{M}' = [1 \quad 1 \quad 0] \quad \text{and} \quad [1 \quad 1 \quad 1 \quad 0] \tag{14}$$

in the plane strain and axisymmetric cases, respectively (${}^{\mathrm{T}}\mathbf{X}$ means the matrix $\mathbf{X}$ is transposed).

The vector $\mathbf{g}'$ of the first derivatives of g with respect to the nodal point velocities $\mathbf{a}$ is now introduced

$$\mathbf{g}' = \sum_{i=1}^{N_e} \int_{V_i} \{\sigma({}^{\mathrm{T}}\mathbf{a}\mathbf{B}\mathbf{a})^{(m-1)/2}\mathbf{B}\mathbf{a} + \rho\mathbf{B}'\mathbf{a}\}\,\mathrm{d}V \tag{15}$$

where $\mathbf{B} = {}^{\mathrm{T}}\mathbf{N}'\mathbf{M}\,\mathbf{N}'$ and $\mathbf{B}' = {}^{\mathrm{T}}\mathbf{N}'\mathbf{M}'{}^{\mathrm{T}}\mathbf{M}'\mathbf{N}'$. A vector $\tilde{\mathbf{g}}'$ can be formed with the components of $\mathbf{g}'$ corresponding to the derivatives with respect to the *unknown* nodal point velocities (i.e. which are not prescribed by boundary conditions) and thus the minimization of g can be replaced by the equation

$$\tilde{\mathbf{g}}' = \mathbf{0}. \tag{16}$$

Equation (16) was solved in an iterative manner by using a Newton–Raphson method starting from the velocity field $\mathbf{a}^0$ which is readily obtained for $m = 1$ (linearly viscous behaviour), since eqn (16) is linear in this case. Calculations end at the nth iteration when $\|\tilde{\mathbf{g}}'(\mathbf{a}^n)\|$ and $\|\mathbf{a}^n - \mathbf{a}^{n-1}\|/\|\mathbf{a}^{n-1}\|$ are small enough. The integrals in eqn (16) were evaluated with Gaussian quadratures. The first part of the integrand was treated with a four-point quadrature and thus the corresponding integral is calculated exactly for quadratic functions of x and y (which is the case for linearly viscous materials in plane strain only). The second part of the integrand was calculated at the central point of each element only, this means

that dilatation rate (and hydrostatic pressure, according to eqn (7)) was assumed to be constant throughout each element. This reduced integration scheme for the penalty term is well known to improve the results[27, 28].

Calculation of finite strain

The problem of finite strain with this formulation consists in the derivation of the displacement field x from the equation $dx/dt = v$ where v is the velocity field derived according to the variational principle (1). Over a time step δt, the displacement increment δx can be calculated by a classical method (e.g. a Runge–Kutta method, etc.). Thus the new positions of nodes can be updated at each time step. In this paper we are interested in the determination of stresses around the inclusion at the initial stage of deformation. According to flow rules (5) and (7) it appears that the velocity field need only be derived. Thus we do not present any results of finite strain as well as changes in form of the inclusion.

4. INTERFACE STRESS CALCULATION

When eqn (16) is solved, an optimal velocity field is obtained and the associated stress tensor is available at the integration points only where the strain rate tensor and hydrostatic pressure were calculated. Extrapolating stresses from integration points leads to discontinuities across inter-element boundaries and at nodal points where stresses are desired in many problems such as damage initiation. Duvaut and Pistre[29] have previously developed a method for the calculation of tractions applied to *inter-element boundaries* in the case of elastic composite materials. The method which is proposed in this paper is devoted to the derivation of surface tractions at *nodal points* where maximal values can occur in the inclusion problem (Section 5). Although the present study is restricted to inclusion–matrix interface stresses with emphasis on the normal component (which is related to inclusion–matrix decohesion and thus to damage initiation), its field of application is more general and includes the derivation of contact stresses on tools in forming processes.

The principle of virtual work relates surface tractions to self-equilibrated stress tensors defined in the corresponding volume. The finite element analysis of Section 3 leads to a discontinuous interpolated field of stress tensor which does not satisfy the equilibrium equations, but an approximation of the surface tractions applied to a closed surface can nevertheless be obtained through a relation similar to the principle of virtual work as shown below. This method has the advantage of giving the same values whatever the side of the surface which is considered but it should be emphasized that it is not an *application* of the principle of virtual work, the corresponding equation is only used as a *definition* of the calculated surface tractions.

Let $\partial\Omega$ and $\mathbf{c}$ denote the surface of the inclusion (with outer normal n_j) and the vector of the unknown components of surface tractions applied to the nodal points on $\partial\Omega$, respectively. The following discretization can be used to define the surface traction at any point of $\partial\Omega$ by using a linear interpolation

$$\sigma_{ij} n_j = \tilde{\mathbf{N}}\mathbf{c} \tag{17}$$

where $\tilde{\mathbf{N}}$ is the matrix of interpolating functions for the nodal points located on $\partial\Omega$ ($\tilde{\mathbf{N}}$ is a part of matrix $\mathbf{N}$ introduced in Section 3). For any velocity field $\mathbf{v}^*$ defined in Ω by $\mathbf{a}^*$ through a relation similar to eqn (8), the following relationship is obtained

$$\int_{\partial\Omega} \sigma_{ij} n_j v_i^* = {}^{\mathrm{T}}\tilde{\mathbf{a}}^* \mathbf{S}\mathbf{c} \tag{18}$$

where $\tilde{\mathbf{a}}^*$ is a part of $\mathbf{a}^*$ formed by the nodal point velocities on $\partial\Omega$ and

$$\mathbf{S} = \sum_{i=1}^{N_b} \int_{\partial\Omega_i} {}^{\mathrm{T}}\tilde{\mathbf{N}}\tilde{\mathbf{N}}\,\mathrm{d}S \tag{19}$$

where N_b is the number of element boundaries $\partial\Omega_i$ on $\partial\Omega$. S was calculated with a four-point Gaussian quadrature in the present case.

Using the stress tensor associated with the velocity field obtained in Section 3, the following expression can be deduced

$$\int_\Omega \sigma_{ij}\dot{\varepsilon}_{ij}^*\,\mathrm{d}V = {}^{\mathrm{T}}\tilde{\mathbf{a}}^*\tilde{\mathbf{g}}'_\Omega \tag{20}$$

where $\tilde{\mathbf{g}}'_\Omega$ is the vector formed by the first derivatives of the functional g_Ω (defined by eqn (12) where integration is performed over Ω only) with respect to the nodal point velocities on $\partial\Omega$. The zero value of the derivatives of g_Ω with respect to the other nodal point velocities in Ω was used in the derivation of eqn (20) and yields from eqn (16) and from the dependence of the velocity field in an element on the velocities at the four adjacent nodal points only.

The method which is proposed for the calculation of c consists in writing that the integrals in eqns (18) and (20) are equal, which is similar to the virtual work principle equation and takes the following discretized form

$${}^{\mathrm{T}}\mathbf{a}^*\mathbf{S}\mathbf{c} = {}^{\mathrm{T}}\mathbf{a}^*\mathbf{g}'_\Omega. \tag{21}$$

Equation (21) being true for any choice of $\mathbf{a}^*$, c is immediately deduced

$$\mathbf{c} = \mathbf{S}^{-1}\mathbf{g}'_\Omega. \tag{22}$$

An important property of the c value calculated in this way arises when $\partial\Omega$ is considered as part of the surface of the complementary volume V. S depends on the nodal points on $\partial\Omega$ only and is obviously unchanged, a functional g_V is introduced in a similar manner as g_Ω above and the following relationship is obtained

$$g_V + g_\Omega = g. \tag{23}$$

Equations (23) and (16) lead to

$$\mathbf{g}'_V = -\mathbf{g}'_\Omega \tag{24}$$

where $\mathbf{g}'_\Omega$ is defined in a similar way as $\mathbf{g}'_\Omega$ above. It is then concluded from eqn (22) that c values obtained by the proposed method when V and Ω are alternatively considered are exactly opposite, and thus the surface traction equilibrium is satisfied. Equation (22) provides a satisfactory deconvolution of nodal forces and this method is easily implemented in a finite element computer program since S is readily calculated and $\mathbf{g}'_\Omega$(or $\mathbf{g}'_V$) is immediately reckoned.

The above variational formulation, finite element analysis and stress calculation were limited to the inclusion problem for the sake of clarity. It is possible to extend them to more general cases with the help of the following remarks.

(1) Equation (1) applies when displacement rates only are prescribed on the material surface and an extra term must be added to eqns (1), (12) and (15) if surface tractions are prescribed over a portion of this surface. This term is zero when the prescribed surface tractions are zero, which is the case in Sections 6 and 7 below where shear stresses are zero along the left and lower sides of the grid by the virtue of symmetry.

(2) It was assumed implicitly in the derivation of eqn (22) that the surface $\partial\Omega$ was entirely surrounded by the matrix. A similar formula can be found easily in the case where $\partial\Omega$ includes a portion of the outer surface of the material. In these conditions, an extra term corresponding to the prescribed tractions on this surface, if any, must be added to the right-hand side of eqn (18), and eqn (22) is obtained as well. It is also possible to derive the contact stresses on tools in forming processes by applying eqn (22) to the whole outer surface of the material and considering the prescribed velocity boundary conditions as free parameters.

5. SOME ASPECTS OF THE ANALYTICAL SOLUTION FOR A LINEARLY VISCOUS MATRIX

The exact solution of the problem can be derived analytically in the case of an unbounded *linearly* viscous matrix uniformly loaded at infinity surrounding an ellipsoidal power law viscous inclusion. The derivation is detailed in Refs [11, 30] and the particular case of a linearly viscous inclusion was obtained in Refs [31, 32] from Eshelby's solution[1] in elasticity by using the analogy between problems in elasticity and viscosity. Only the main features of the solution are recalled in this paper in order to show the peculiarities of the inclusion problem and the necessity of a close study of the mesh. The following discussion is moreover focused on the simple cases where the symmetry axes of the inclusion and the principal axes of the prescribed loading of the matrix coincide. Some more details on the analytical solution are given in the appendix.

The most outstanding property is the homogeneity of deformation within the inclusion if the following conditions are fulfilled: (a) the matrix is unbounded and homogeneously loaded at infinity, (b) the matrix behaviour is linear (elastic, viscoelastic, viscous), (c) the inclusion shape is an ellipsoid. In the present case this leads to the uniformity of strain rate in the inclusion which is given by

$$\frac{2\lambda}{1+\lambda^2}(\Sigma\delta^{m_I}-1)+\delta-1=0 \quad \text{and} \quad F(\lambda)(\Sigma\delta^{m_I}-1)+\delta-1=0 \tag{25}$$

in the plane strain and axisymmetric cases, respectively. In the above equations the ratio δ of the (uniform) effective strain rate in the inclusion $\dot{\bar{\varepsilon}}_I$ and the prescribed equivalent strain rate at infinity $\dot{\bar{\varepsilon}}_\infty$ was introduced. Σ is the "hardness ratio" defined as the ratio of the inclusion and matrix effective stresses for the prescribed strain rate $\dot{\bar{\varepsilon}}_\infty$, i.e. $\Sigma = \sigma_I \dot{\bar{\varepsilon}}_\infty^{m_I - m_M}/\sigma_M$ ($m_M = 1$ in the present case). λ is the inclusion aspect ratio defined as the ratio of the inclusion radii along the y- and x-axes, respectively. F is a function of λ which is detailed in Ref. [11] and takes the value 2/3 for $\lambda = 1$ (spherical inclusion).

It is worthwhile to notice that strain rate is not continuous across the inclusion–matrix interface (except along the coordinate axes) although velocity is. This property is particular to multiphased media (see strain rate jump calculation in Ref. [11]) and requires a special study of the mesh on both sides of the interface. Steep strain rate gradients occur just outside the inclusion and thus thin elements are required in this area, especially around the inclusion tips in the case of large aspect ratios. The strain rate in the matrix approaches the prescribed value at infinity (more rapidly in the axisymmetric case than in plane strain) with increasing distance from the inclusion and this allows the use of elements increasing in size. It should be added that the hydrostatic pressure variations are qualitatively similar to those described above for strain rate, the uniform value p_I in the inclusion is given by

$$p_I = p_\infty \pm \frac{1}{\sqrt{3}}\sigma_M \dot{\bar{\varepsilon}}_\infty \frac{1-\lambda^2}{1+\lambda^2}(\Sigma\delta^{m_I}-1)$$

and (26)

$$p_I = p_\infty \pm \frac{2}{3}\sigma_M \dot{\bar{\varepsilon}}_\infty \frac{1-\lambda^2}{1+2\lambda^2}(\Sigma\delta^{m_I}-1)$$

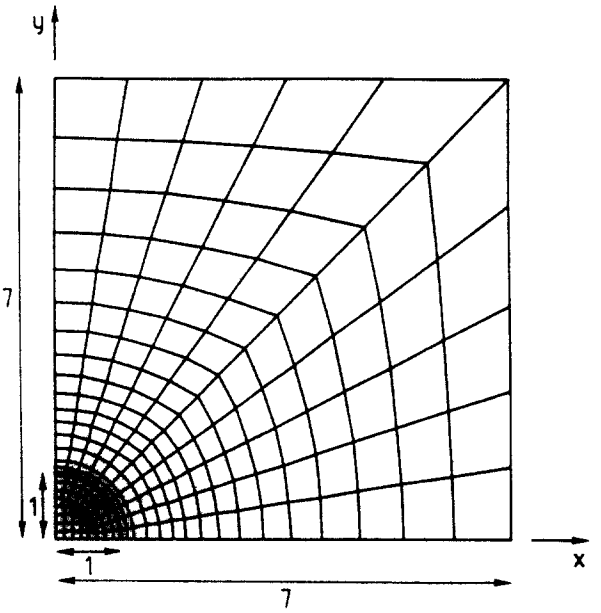

Fig. 1. General view of the final grid.

in the plane strain and axisymmetric cases, respectively. In the above equations p_∞ is the prescribed hydrostatic pressure at infinity, the plus (resp. minus) sign refers to a tension (resp. a compression) along the y-axis. Equations (26) show that the hydrostatic pressure in the inclusion equals the value at infinity in the case of a circular cylindrical or spherical inclusion ($\lambda = 1$).

As a consequence of stress uniformity in the inclusion and surface traction continuity across the interface, the stress component normal to the interface reaches a maximum value along the y-axis in the case of a prescribed plane or axisymmetric uniaxial tension in that direction. Its value is given by

$$\frac{\sigma_{rr}}{\sigma_\infty} = \frac{1 + \Sigma\delta^{m_i}\lambda^2}{1 + \lambda^2} \quad \text{and} \quad \frac{\sigma_{rr}}{\sigma_\infty} = \frac{1 + 2\Sigma\delta^{m_i}\lambda^2}{1 + 2\lambda^2} \tag{27}$$

in the plane strain and axisymmetric cases, respectively. In the above equations σ_∞ is positive and denotes the prescribed tensile stress at infinity.

The exact analytical solution in the case of a linearly viscous matrix shows moreover that the velocity components in the matrix are not polynomials of x and y[11], this means that the exact solution cannot be obtained with the proposed finite element method but the disagreement can nevertheless be reduced by a good choice of grid. Additional errors are moreover introduced by numerical quadratures and data rounding up. The latter factor was reduced by using the double precision data type in the present computer program. The best agreement between the analytical and finite element solutions is liable to occur in the case of a circular cylindrical inclusion in plane strain and these are the conditions of the following grid tests.

6. TESTS AND MESH OPTIMIZATION (LINEARLY VISCOUS MATERIALS)

By virtue of the dictated symmetry of the matrix and inclusion deformation, only one quadrant need be studied. The following tests were performed in the case of *linearly* viscous materials, where the exact analytical solution is available. The matrix infinite extension is modelled by setting the velocities on the nodal points of the (finite) mesh boundaries equal to the corresponding values given by the analytical solutions on these points. Figure 1 shows a general view of the grid, the sides of which are seven times the inclusion radius

long. Several preliminary tests were performed so as to obtain the best fit with the analytical solution as possible, and are described below.

A first way of meshing the inclusion area is shown in Fig. 2(a). The use of circular rings (see e.g. Ref. [33] for a similar problem with elastic–plastic materials) introduces necessarily a core at the centre of the inclusion, on which boundary conditions must be chosen. In the present case, the core radius was 2% of the inclusion and the velocities were set equal to zero on its boundary because of the null velocity of the inclusion centre. Figures 2(b)–(d) show that the introduction of a small hard core in the inclusion induces a noticeable strain rate inhomogeneity in the latter and a discrepancy with the analytical solution: in the case of a soft inclusion ($\Sigma = 0.5$) the strain rate in the inclusion varies from -11.98 to 7.6% around the average value which is 0.38% below the theoretical (uniform) value given by eqn (25). This kind of mesh is consequently not suitable for the specific problem which is studied in this paper, but it can nevertheless be used for the duplex inclusion problem (which has not been solved analytically). It is worthwhile to notice that the strain rate inhomogeneity induced in the inclusion by the rigid central core has the same aspect as the one induced by a hard inclusion in a soft matrix[11]: areas of higher (resp. lower) values are located on the axes (resp. their bisectors).

A second kind of mesh was tested, which does not introduce the above-mentioned problem at the inclusion centre (Fig. 3(a)). One element has necessarily a quasi-triangular shape but it was checked that this had no influence on the results. This kind of mesh was used, for instance, in Ref. [23]. The agreement with the exact solution is much better than for the first mesh, in the same conditions: the strain rate in the inclusion varies from -0.24 to 0.23% around the average which is 0.29% below the theoretical value. The strain rate inhomogeneity in the inclusion is located below the interface (Fig. 3(b)). This is due to the strain rate discontinuity across the interface mentioned in Section 5 and to the interpolation of effective strain rate in Fig. 3(b). The agreement with the theoretical values is also improved for the strain rate in the matrix (Figs 3(c) and (d)).

In order to obtain the best fit with the analytical solution as possible, a third mesh was eventually considered and adopted. The difference with the second mesh lies on the addition of circular rings of thin elements on both sides of the inclusion–matrix interface (Fig. 4(a)). The strain rate homogeneity within the inclusion is well satisfied: the variations extend from -0.24 to 0.18% around the average which is 0.23% below the theoretical value (Fig. 4(b)). The agreement is also satisfactory in the matrix (Figs 4(c) and (d)). The interpolative description of the strain rate in the finite element analysis described in Section 3 is not continuous across inter-element boundaries (although the velocity is) but the present tests show that this is not enough to cope with the strain rate jumps at the interface in the inclusion problem and, consequently, thin elements must be used in this area. As the same main features are obtained with other material behaviours when the exact solution is available, it can be inferred that meshes without a central core and with thin elements on both sides of the interface should be used generally for the deformable inclusion problems.

The final mesh (Figs 1 and 4(a)) contained 267 nodes and 235 elements, including 65 in the inclusion, with a total number of 460 degrees of freedom. Further tests with nine-node elements were also performed to account for the circular shape of the inclusion, for the polygonal approximation of the interface with four-node elements could be a cause of misfit with the analytical solution. This increased the program size and complexity without leading to any significant improvement in the results.

Noticeably worse results were found in the case of axial symmetry than in plane strain. A region of low strain rate values was obtained under the pole of soft inclusions (and high values for hard inclusions) and the strain rate variations ranged from -5.93 to 1.85% around the average which was 0.99% below the theoretical value in the same conditions as the above plane strain tests (Fig. 5(a)). Figures 5(b) and (c) show that the strain rate variations in the matrix were well predicted along the x-axis and the axes bisector, but the results were worse along the symmetry axis (Fig. 5(d)). The addition of

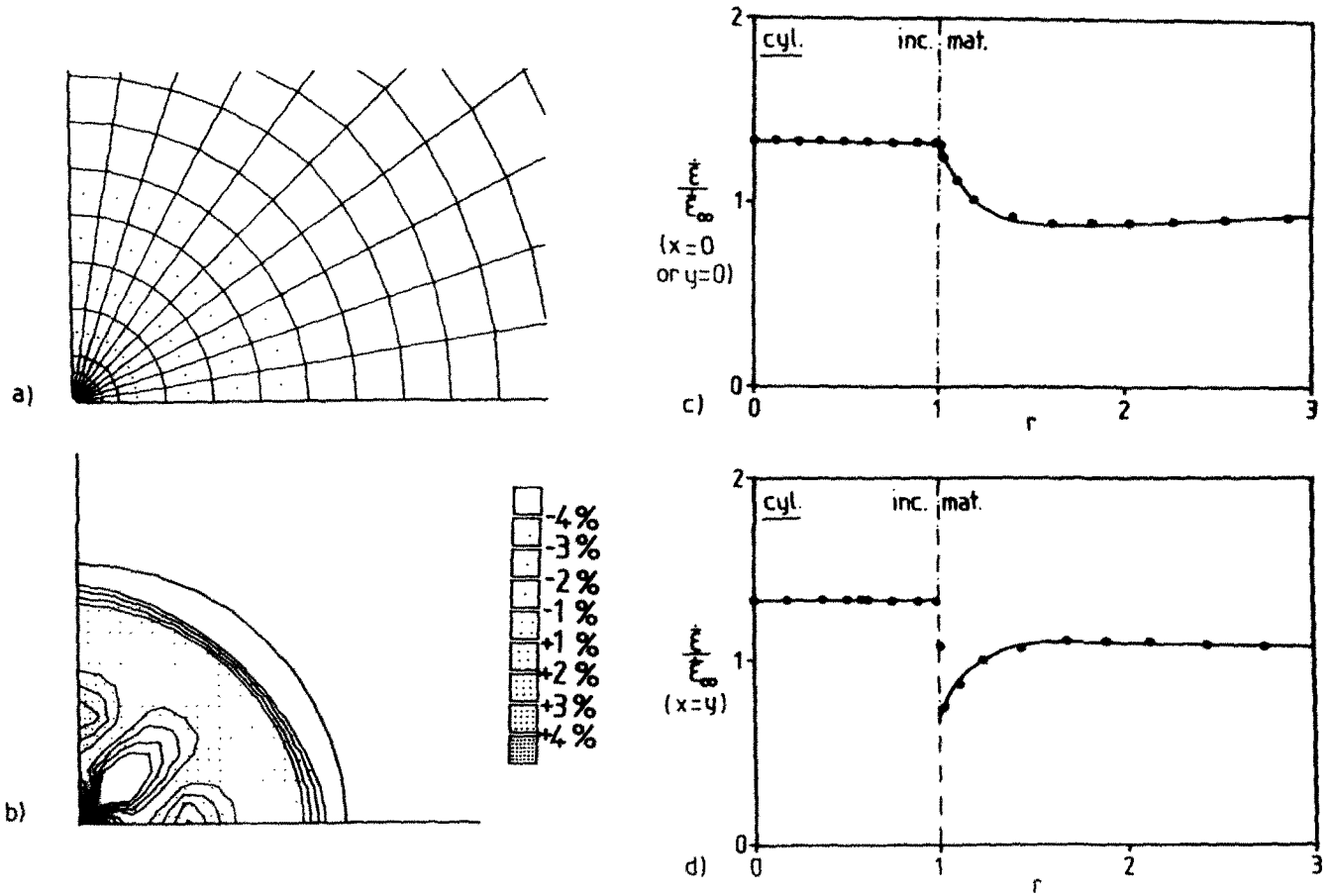

Fig. 2. Tests of the first mesh (231 nodes, 200 elements including 50 in the inclusion): enlargement of the inclusion area (a); effective strain rate contours in the inclusion (b); distribution (dots) along the axes (c) and the bisector (d), comparison with theoretical values (solid lines) as a function of the distance from the inclusion centre (r). Linearly viscous materials in plane tension along the vertical axis, soft inclusion ($\Sigma \approx 0.5$). The contours on map (b) are normalized by the average effective strain rate in the inclusion and the indicated scale is used.

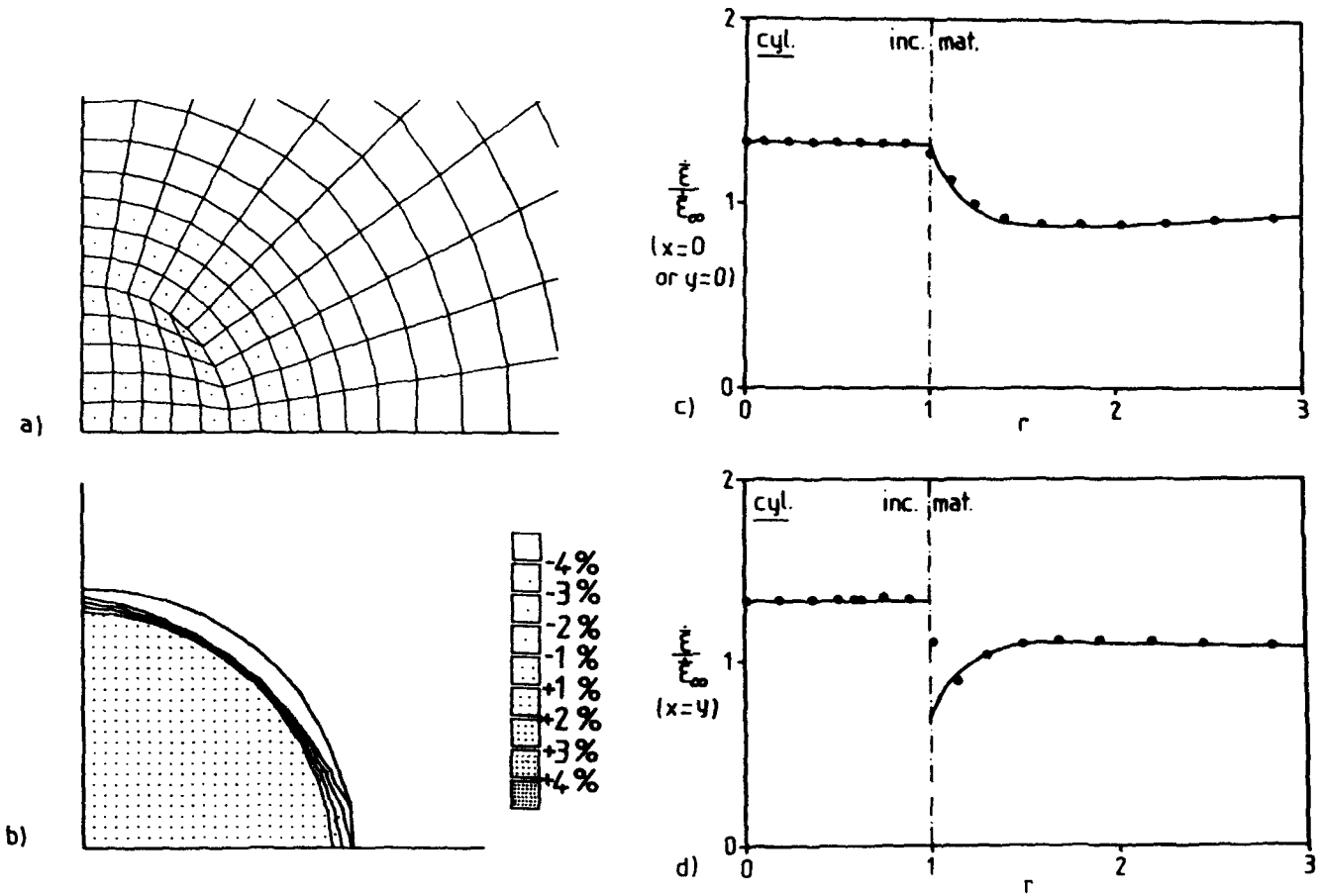

Fig. 3. Same as Fig. 2 for the second mesh (245 nodes, 215 elements including 55 in the inclusion).

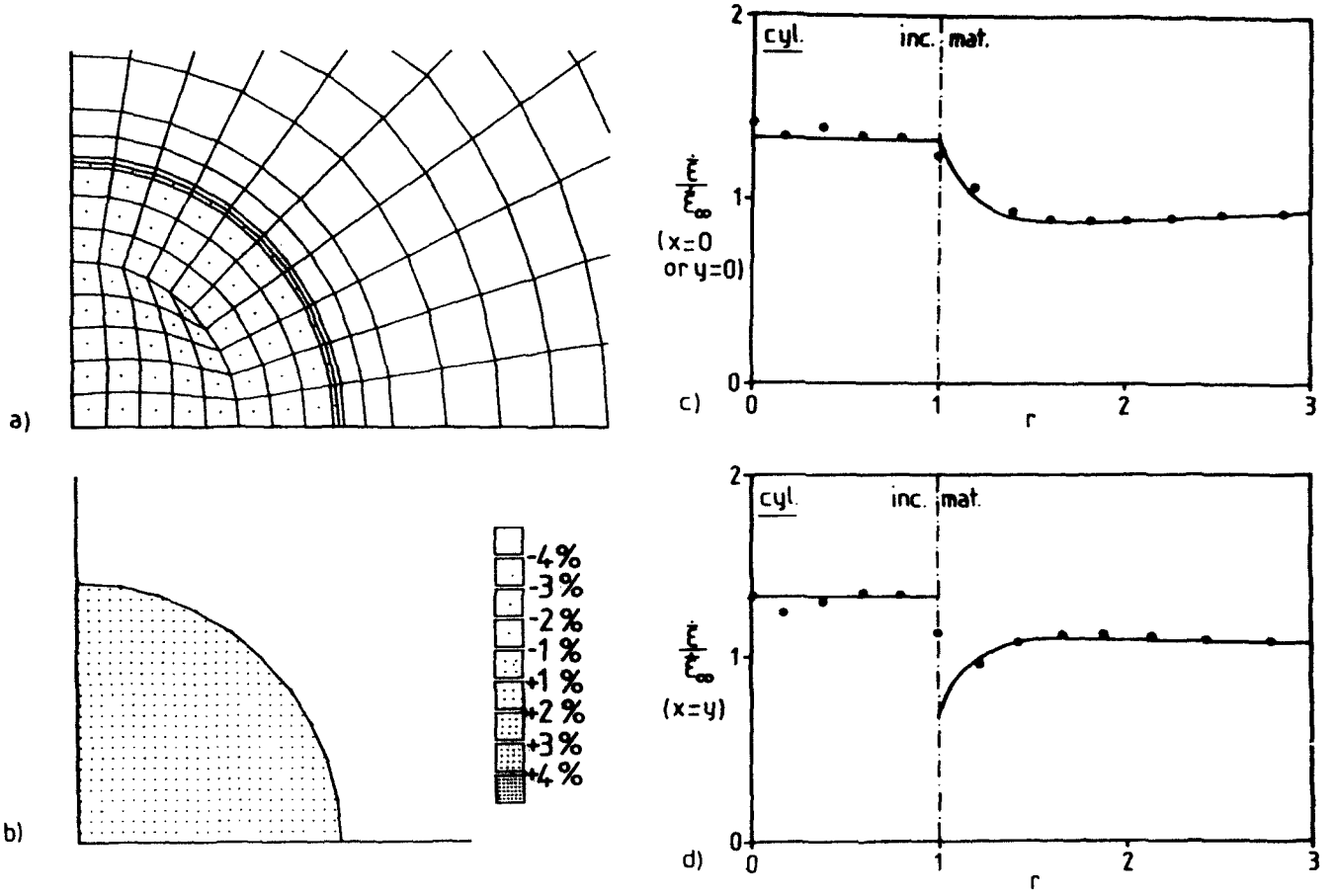

Fig. 4. Same as Fig. 2 for the final mesh (267 nodes, 235 elements including 65 in the inclusion).

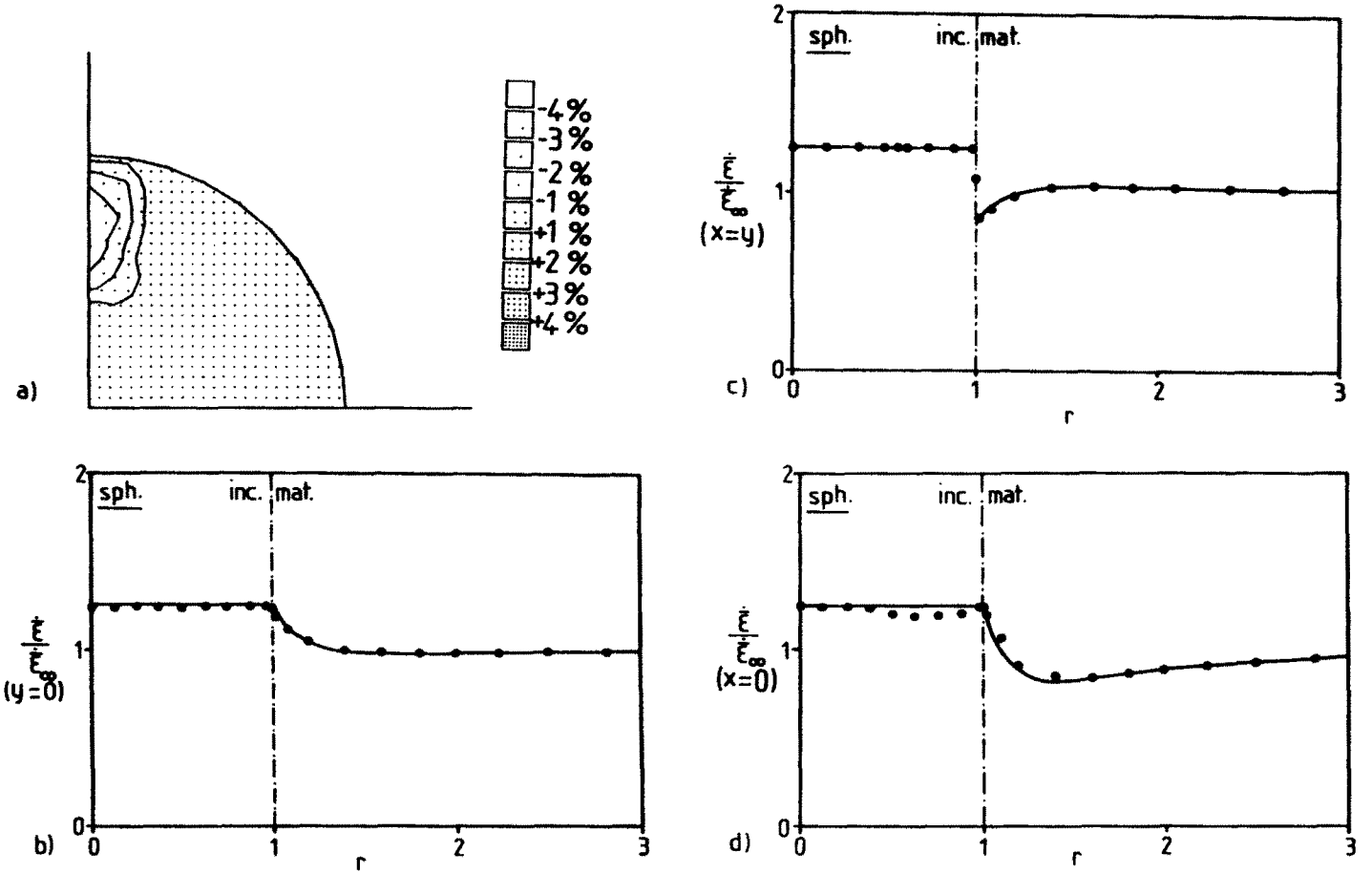

Fig. 5. Test of the final mesh in the case of axial symmetry around the vertical axis: (a) effective strain rate contours in the inclusion (same scale as Fig. 2); distribution along the x- axis (b), the bisector (c), and the y-axis (d). Linearly viscous materials, soft inclusion ($\Sigma = 0.5$).

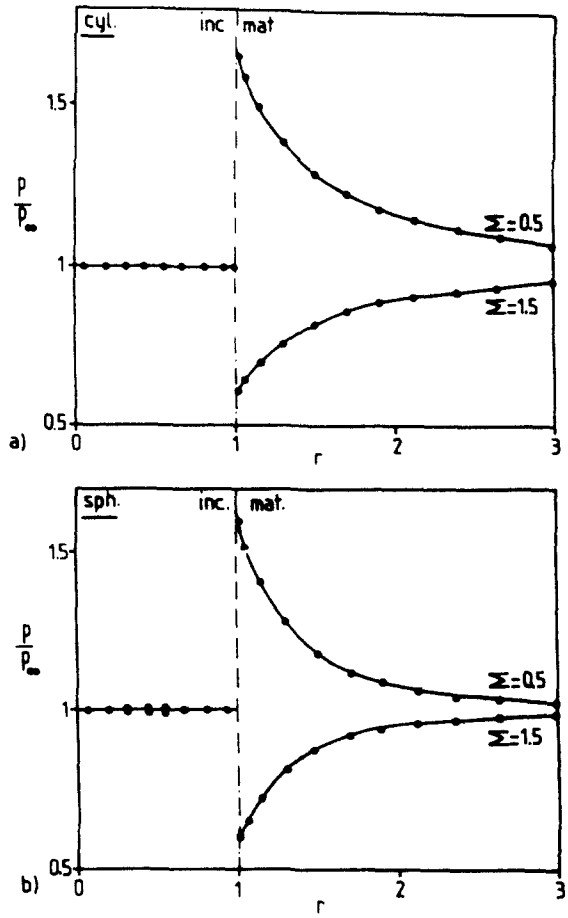

Fig. 6. Hydrostatic pressure along the axes in plane strain (a) and along the x-axis in the axisymmetric case (b), normalized by the prescribed value at infinity. Comparison between the finite element results (dots) and the theoretical values (solid lines). Linearly viscous materials, soft ($\Sigma = 0.5$) or hard ($\Sigma = 1.5$) inclusion, uniaxial tension at infinity.

two rows of thin elements along this axis was tried but did not lead to significantly better results.

Figures 6(a) and (b) confirm the validity of the hydrostatic pressure calculation by using eqn (7). The agreement with the theoretical values was very satisfactory in the plane strain case as well along the axes (Fig. 6(a)) as along their bisectors where a constant value was obtained. The results were still good on the x-axis in the axisymmetric case (Fig. 6(b)) but similar problems as those mentioned above were found along the y-axis. The predictions of the stress component normal to the interface were also checked (Table 1): very good results were obtained in the plane strain case for all the nodal points on the interface, but a misfit occurs on the y-axis only in the axisymmetric case for which the values obtained 9° from this axis are considered in the following.

In the general case of a non-linearly viscous matrix, the lack of an exact analytical solution makes it impossible to simulate an infinite matrix by imposing convenient boundary conditions at a finite distance from the inclusion as in the above tests. The velocities on the nodal points of the upper and right sides of the mesh were consequently set equal to those corresponding to a homogeneous deformation. Then the problem was of a finite matrix containing an inclusion or, in the plane strain case, of a doubly periodic array of cylindrical inclusions in an infinite matrix. Although the mesh size was chosen large enough (seven times the inclusion radius) to consider the matrix was infinite, it was useful to study the influence of this change in the boundary conditions. Table 1 shows that the perturbation of the results was more important in the plane strain case, and this can be explained easily by the greater mesh inclusion content (1.60%) than in the axisymmetric

Table 1. Influence of the matrix size on the average ($\dot{\bar{\varepsilon}}_i$) and variations of the strain rate in the inclusion, and on the maximal normal traction at the interface (σ_{rr}). Uniaxial tension prescribed to the matrix, linearly viscous materials

			Discrepancy between the calculated average $\dot{\bar{\varepsilon}}_i$ and exact solution (%)	Variations of $\dot{\varepsilon}$ in the inclusion around the average (%)		Discrepancy between the calculated value of σ_{rr} and exact solution (%)
Soft inclusion ($\Sigma = 0.5$)	cylinder	infinite matrix	−0.26	−0.24	0.18	0.51
		finite matrix	−2.31	−0.21	0.16	−0.33
	sphere	infinite matrix	−0.99	−5.93	1.85	−0.80
		finite matrix	−1.38	−6.51	1.74	−0.84
Hard inclusion ($\Sigma = 1.5$)	cylinder	infinite matrix	0.17	−0.11	0.15	0.76
		finite matrix	1.44	−0.09	0.13	1.47
	sphere	infinite matrix	0.69	−1.16	3.77	−0.81
		finite matrix	0.96	−1.13	3.93	−0.73

case (0.19%). It is concluded from these tests that, as far as the problem of a unique inclusion in an infinite viscoplastic matrix is concerned, a relative precision of 2 or 3% for the average strain rate in the inclusion and 1% for the stress concentration at the interface can be expected from the finite element calculations. The strain rate inhomogeneity in the inclusion should only be considered as significant over $\pm 0.2\%$ in the plane strain case and $\pm 5\%$ in the axisymmetric case. It should be added that these figures are only orders of magnitude and can be considered as minimal values, for it is known that a decrease in the power law exponent enhances generally the flow inhomogeneity and thus the effect of the finite size of the matrix is expected to increase.

A convenient way of varying the inclusion aspect ratio λ is to multiply the y-coordinate of all the nodal points of the mesh by λ. Figure 7 shows the results which were obtained for various oblate ($\lambda < 1$) or prolate ($\lambda > 1$) inclusions in the same conditions as above. The discrepancy with the theoretical results increases when the aspect ratio departs from unity, due to the very steep strain rate gradients induced near the inclusion tips which would require a much thinner mesh in these areas and more memory space and computational time consequently[11]. The $\lambda = 2$ and 1/2 cases are nevertheless considered in the following, since the agreement with theory is still acceptable and because the influence of the inclusion aspect ratio is significant in these conditions.

7. RESULTS (POWER LAW VISCOUS MATERIALS)

The finite element program which is proposed here and which has been tested as described above, was applied to several cases of inclusion problems for power law viscous materials in plane strain or axially symmetric deformation. Various aspect and hardness ratios were considered and the rate hardening coefficient was varied with an equal value in the inclusion and the matrix in order to restrict the number of cases which was nevertheless more than a hundred. The value of the rate hardening coefficient in both materials is denoted by m in the rest of this paper.

The computation time rapidly increased for decreasing values of m (Fig. 8) due to an increasing number of iterations before the convergence was obtained. For small values of m (< 0.2), the iterative procedure diverged and two different methods were used to improve the calculation.

(1) The first method consisted in changing the starting velocity field in the iterative process by using the approximative velocity field deduced from a variational method proposed elsewhere[11] for power law viscous materials, instead of using the solution obtained for linearly viscous materials as mentioned above.

(2) When this procedure did not lead to convergence, the flow rule was modified in the following way

$$s_{ij} = \frac{2}{3}\sigma(\dot{\bar{\varepsilon}} + \dot{\bar{\varepsilon}}_0)^{m-1}\dot{\varepsilon}_{ij} \tag{28}$$

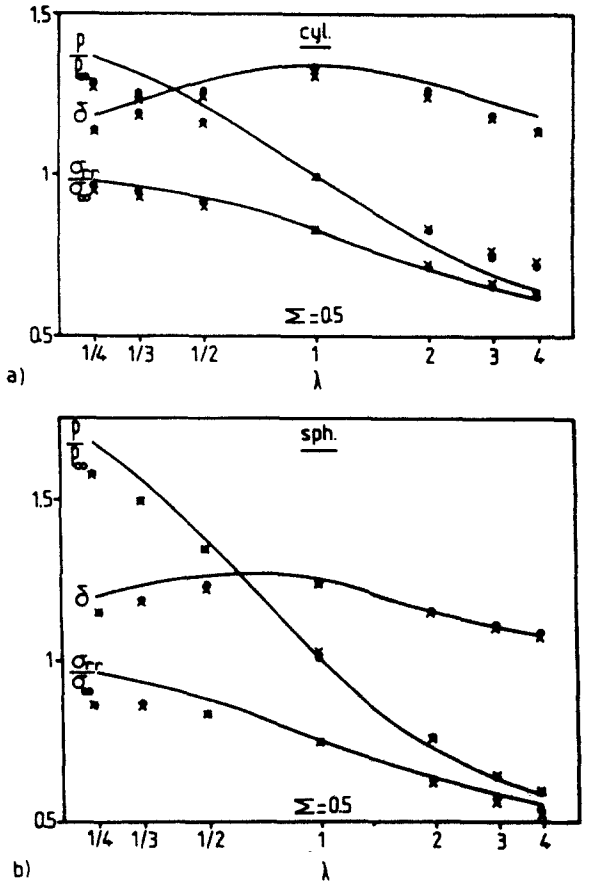

Fig. 7. Comparison between theoretical values (solid lines) and finite element results (dots: unbounded matrix, crosses: finite matrix) for various aspect ratios (λ). Average effective strain rate (δ) and hydrostatic pressure (p/p_∞) in the inclusion, maximal interface traction ($\sigma_{rr}/\sigma_\infty$) normalized by the corresponding values at infinity. Linearly viscous materials, soft inclusion ($\Sigma = 0.5$), uniaxial tension applied to the matrix in plane strain (a) or axisymmetric deformation (b).

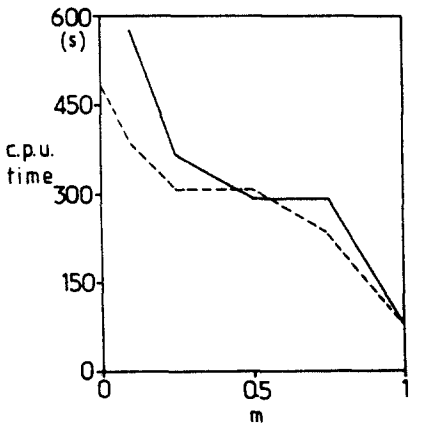

Fig. 8. Variation of the central processing unit computation time on a Perkin Elmer 3220 computer with the rate hardening coefficient of the two materials (m). Cylindrical (solid line) or spherical (broken line) soft inclusion ($\Sigma = 0.5$).

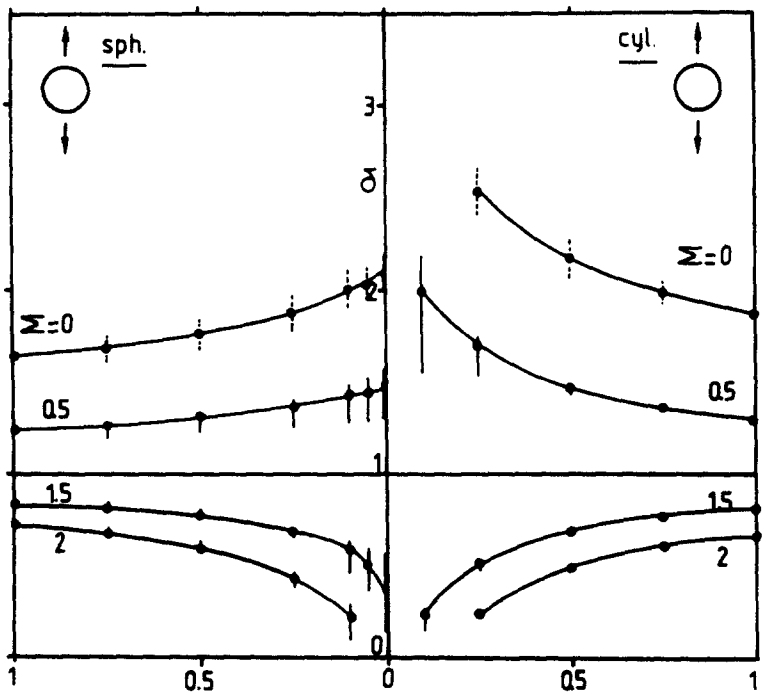

Fig. 9. Average value (dots) and range of variation (bars) of the effective strain rate in the inclusion (normalized by the prescribed value at the mesh boundary) for various values of the rate hardening coefficient taken equal in both materials (m) and various hardness ratios. Spherical (left) or cylindrical (right) inclusion.

which is known to improve the convergence for small m values. $\dot{\bar{\varepsilon}}_0$ was chosen small enough (10^{-3}) to limit the departure from the original material behaviour (eqn (5)). Thus it was sometimes even possible to obtain results for $m = 0$, but this does not represent strictly the case of perfect plasticity, since no yield criterion is considered in the present finite element analysis.

The use of the above two methods enlarged the range of m values where results could be obtained, but divergence still occurred in some cases of small m values, for which no general rule could be derived. Other problems were found for extreme hardness ratios.

(1) The case of an inviscid inclusion ($\Sigma = 0$) could not be treated exactly because of zero terms occurring in the stiffness matrix, and was consequently approximated by $\Sigma = 0.001$.

(2) The case of a rigid inclusion ($\Sigma \to \infty$) could not be considered either, because a finite value must be given to Σ in the present program which, if too great, can lead to excessive differences in the order of magnitude for terms in the stiffness matrix. The hardness ratio was consequently increased until the average strain rate in the inclusion was small enough ($< 10^{-2}\dot{\bar{\varepsilon}}_\infty$), but divergence occurred for $m < 0.5$. This procedure was found more convenient than changing the boundary conditions (zero velocity on the interface) and adapting the stress calculation consequently.

7.1. *Strain rate in the inclusion*

Figures 9–11 show the results obtained for the average strain rate in the inclusion (normalized by the prescribed strain rate at the matrix boundary) for various aspect and hardness ratios, in plane strain and axially symmetric deformation. It can be seen that the flow heterogeneity between the matrix and the inclusion tends to increase when the behaviour of both materials departs from linear viscosity: the average strain rate increases (resp. decreases) in a soft (resp. hard) inclusion of given aspect and hardness ratio, thus

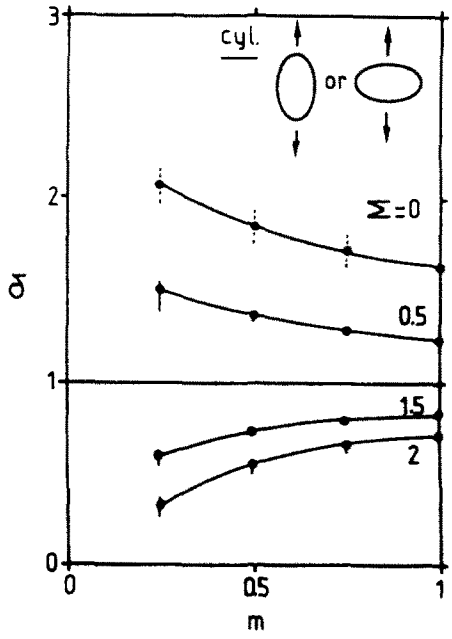

Fig. 10. Same as Fig. 9 for cylindrical inclusions with an aspect ratio equal to 2 or 1/2.

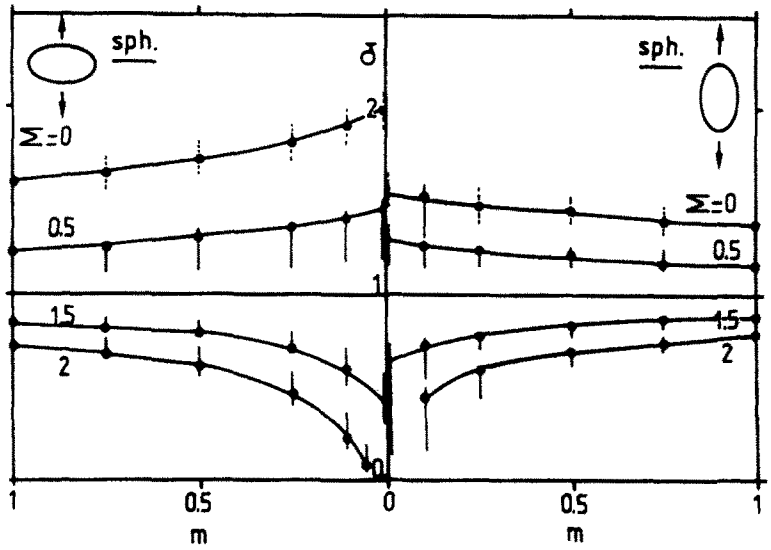

Fig. 11. Same as Fig. 9 for spheroidal inclusions with an aspect ratio equal to 2 (right) or 1/2 (left).

leading to a faster (resp. slower) change in shape when m decreases. This flow heterogeneity between the two materials is lower for a spheroidal inclusion than for a cylindrical one (δ is closer to 1) with the same aspect and hardness ratio, and is reduced when the hardness ratio is closer to 1 or when the aspect ratio departs from 1.

The vertical bars in Figs 9–11 indicate the range of strain rate which was obtained in the inclusion. Thus the noteworthy homogeneity of the deformation in the inclusion is lost when the matrix behaviour is nonlinear, and the strain rate heterogeneity in the inclusion increases with decreasing m. The broken bars used in the case of very soft inclusions in Figs 9–11 ($\Sigma = 0$) only indicate that the strain rate was heterogeneous, since the range of variation was found to be excessive (even for $m = 1$) for this particular hardness ratio. Figure 12 displays the distribution of the strain rate heterogeneity within cylindrical or spherical inclusions for various m values. This heterogeneity is seen to be negligible as far as $m \geqslant 0.25$, it is located at the centre of the inclusion (where high strain rate values

are obtained, be the inclusion softer or harder than the surrounding matrix) and under the interface around the axes bisectors (where low values are obtained). A peak value occurs near the axes bisectors in the case of a cylindrical hard inclusion only (Fig. 12(b)). The interpretation of Figs 12(c) and (d) is more delicate because of an erroneous strain rate heterogeneity under the pole of the inclusion for $m = 1$ as mentioned in Section 6, which spreads in the inclusion with decreasing m in the case of a soft inclusion (Fig. 12(c)) but fades out for a hard one (Fig. 12(d)). Such maps may be a guide for the development of slip line fields solutions in the case of rigid–perfectly plastic materials. (The only case which was previously approached concerned a rigid inclusion in plane strain[13].)

7.2. Maximal normal traction on the interface

It has been recalled in Section 5 that the maximal normal traction on the interface occurs at the pole of the inclusion in the case of a linearly viscous matrix submitted to a uniaxial tension. The present finite element calculations show that the location of this maximum does not change significantly when m is decreased, the only case where it was found 9° from the pole occurred for hard cylindrical inclusions and low m values and the difference from the pole value was small: 1% for $m = 0.1$, $\Sigma = 1.5$ and $\lambda = 1$, for instance. Huang[14] previously found that the radial stress reached a maximum 15° from the pole of the inclusion, 7% higher than the pole value, in the case of a rigid cylindrical inclusion embedded in a matrix with $m = 0.14$. In agreement with this result, the analysis of the present finite element results suggests that this effect is related to the cylindrical shape of the inclusion, high hardness ratios and low m values. It should be added that a possible lowering of the normal traction near the pole of the inclusion could not be discerned easily in the case of spheroidal inclusions because of the above-mentioned problem on the symmetry axis.

Figures 13–15 display the value of the maximal normal traction on the interface normalized by the uniaxial tension prescribed at the matrix boundary, as given by the finite element computation for various aspect and hardness ratios and m values. It appears that the stress concentration does not vary significantly for $0.5 \leqslant m \leqslant 1$ if the inclusion is not too hard, and the analytical solution (eqns (26)) gives consequently a good and quick estimate in this range. For very hard inclusions the stress concentration decreases rapidly with decreasing m. The effect of the aspect ratio is as expected for hard inclusions: the stress concentration increases with increasing aspect ratio, the radius of curvature at the pole of the inclusion being smaller. It should be noticed that the aspect ratio effect is more surprisingly opposite for soft inclusions. This agrees with similar trends which can be deduced from Eshelby's solution for elastic materials.

8. CONCLUSIONS

A finite element program was developed to deal with the inclusion problem in the case of power law viscous materials, based on a penalty method. An original method for the calculation of interface tractions was proposed and included in the program. The necessity of a close study of the mesh was shown and the available exact analytical solution in the case of a linearly viscous matrix was used for this purpose. Many different cases were treated, concerning various aspect and hardness ratios and rate sensitivities, as well in plane strain as in axially symmetric deformation.

The results concern the change in shape of inclusions and damage initiation due to interface decohesion in creep, metals forming in the hot range and superplastic materials.

(1) Soft (resp. hard) inclusions tend to change in shape more (resp. less) rapidly than the surrounding matrix and this difference is enhanced for decreasing rate sensitivities and reduced for oblate or prolate inclusions.

(2) Tensile interface tractions may induce inclusion–matrix decohesion and, in the case of a uniaxial tension prescribed to the matrix, the maximal value is found at (or close to) the pole of the inclusion. Its value is enhanced when the radius of curvature at this

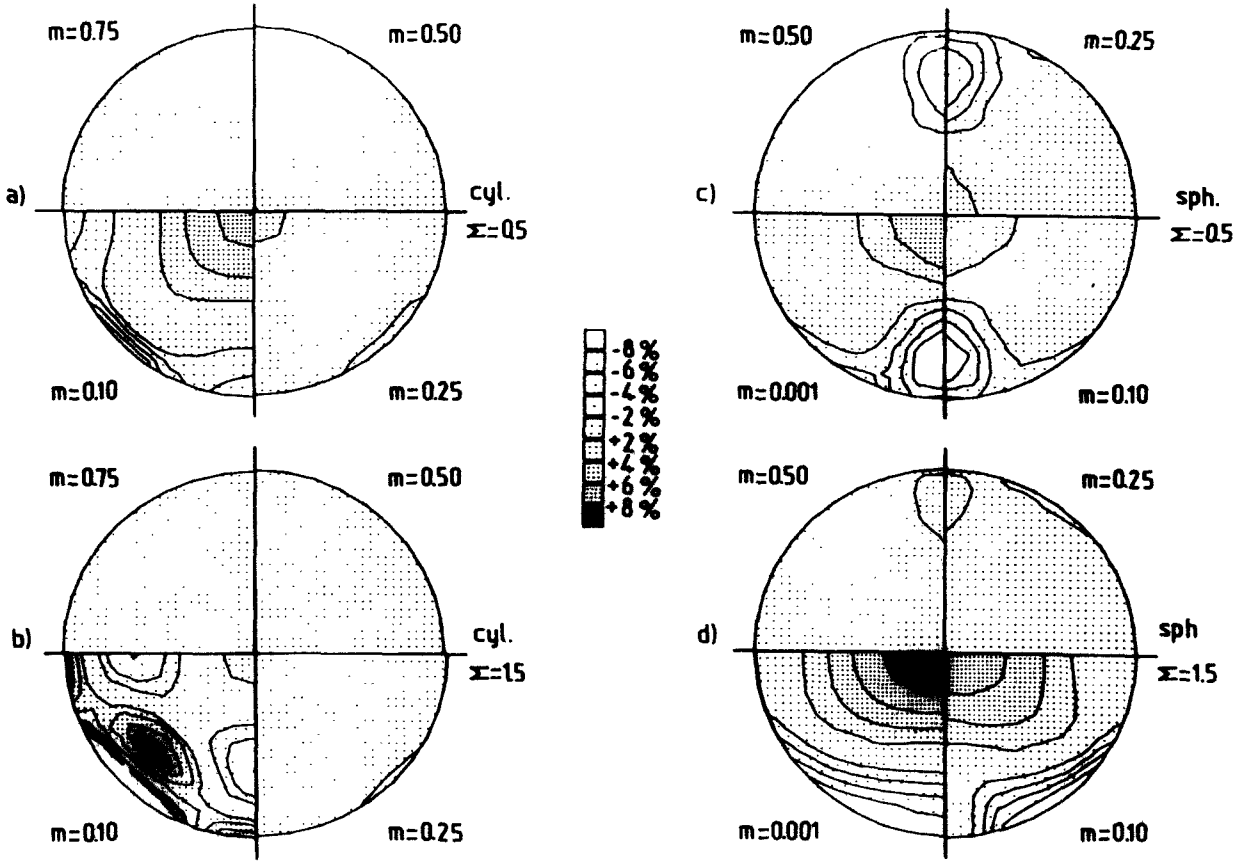

Fig. 12. Effective strain rate contours in cylindrical (a, b) or spherical (c, d) soft ($\Sigma = 0.5$) or hard ($\Sigma = 1.5$) inclusions, for various rate hardening coefficients taken equal in both materials. The contours are normalized by the average value in the inclusion and the indicated scale is used, except for the case $\Sigma = 1.5$ and $m = 0.001$ where 10% instead of 2% steps were used.

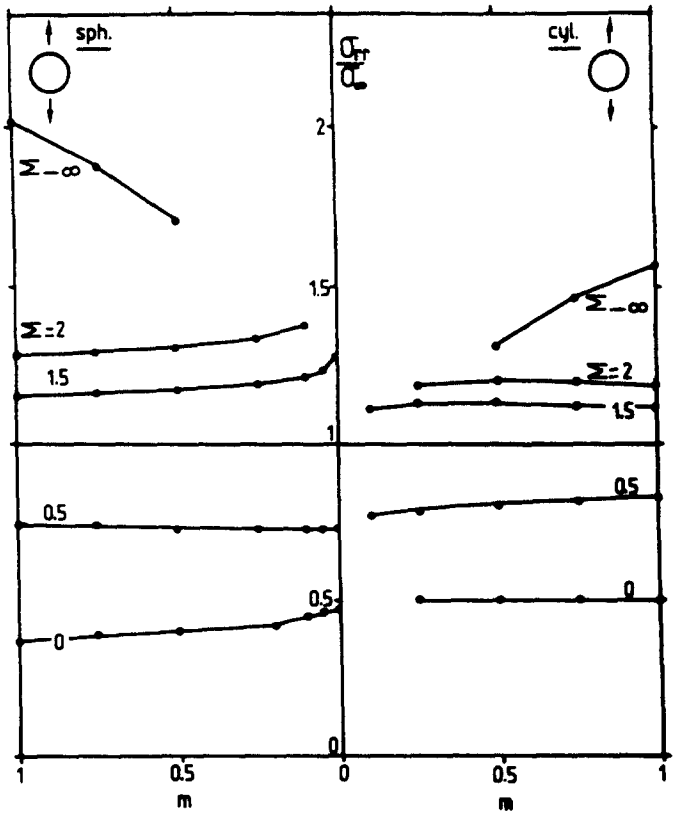

Fig. 13. Maximal normal traction on the interface, normalized by the prescribed uniaxial tension at the matrix boundary, for various rate hardening coefficients and hardness ratios. Spherical (left) or cylindrical (right) inclusion.

point is reduced in the case of hard inclusions, and the opposite for soft ones. The influence of rate sensitivity on the stress concentration is low for soft or moderately hard inclusions, and a decrease in rate sensitivity leads to a decrease in the stress concentration for rigid inclusions.

Acknowledgements—The authors gratefully acknowledge Dr F. Montheillet for stimulating discussions and encouragements during the course of this work.

REFERENCES

1. J. D. Eshelby, The determination of the elastic field of an ellipsoidal inclusion and related problems. *Proc. R. Soc. Lond.* **A241**, 376 (1957).
2. L. J. Walpole, The elastic field of an inclusion in an anisotropic medium. *Proc. R. Soc. Lond.* **A300**, 270 (1967).
3. I. A. Kunin and E. G. Sosnina, Ellipsoidal inhomogeneity in an elastic medium. *Sov. Phys. Dokl.* **16**, 534 (1972).
4. W. C. Johnson, Y. Y. Earmme and J. K. Lee, Approximation of the strain field associated with an inhomogeneous precipitate. *J. Appl. Mech.* **47**, 775 (1980).
5. P. S. Theocaris and N. I. Ioakimidis, The inclusion problem in plane elasticity. *Q. J. Mech. Appl. Math.* **30**, 437 (1977).
6. Z. Hashin, The inelastic inclusion problem. *Int. J. Engng Sci.* **7**, 11 (1969).
7. N. Laws and R. McLaughlin, Self-consistent estimates for the viscoelastic creep compliances of composite materials. *Proc. R. Soc. Lond.* **A359**, 251 (1978).
8. J. R. Rice and D. M. Tracey, On the ductile enlargement of voids in triaxial stress fields. *J. Mech. Phys. Solids* **17**, 201 (1969).
9. A. L. Gurson, Continuum theory of ductile rupture by void nucleation and growth. Part I: yield criteria and flow rules for porous ductile media. *J. Engng Mater. Technol.* **99**, 2 (1977).
10. B. Budiansky, J. W. Hutchinson and S. Slutsky, Void growth and collapse in viscous solids, *Mechanics of Solids. The Rodney Hill 60th Anniversary Volume* (Edited by H. G. Hopkins and M. J. Sewell), p. 13. Pergamon Press, Oxford (1982).

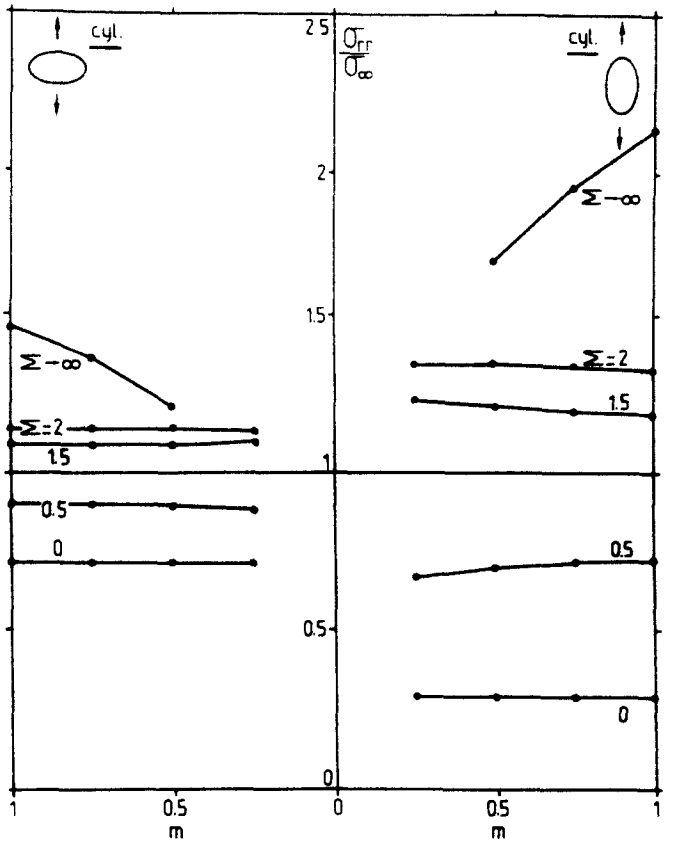

Fig. 14. Same as Fig. 13 for cylindrical inclusions with an aspect ratio equal to 2 (right) or 1/2 (left).

11. P. Gilormini and F. Montheillet, Deformation of an inclusion in a viscous matrix and induced stress concentrations. *J. Mech. Phys. Solids* **34**, 97 (1986).
12. I. S. Tuba, Elastic–plastic analysis of a flat plate with a circular rigid inclusion. *Appl. Scient. Res.* **16**, 241 (1966).
13. J. Orr and D. K. Brown, Elasto-plastic solution for a cylindrical inclusion in plane strain. *Engng Fracture Mech.* **6**, 261 (1974).
14. W. C. Huang, Theoretical study of stress concentrations at circular holes and inclusions in strain-hardening materials. *Int. J. Solids Structures* **8**, 149 (1972).
15. P. V. Marcal and I. P. King, Elastic–plastic analysis of two-dimensional stress systems by the finite element method. *Int. J. Mech. Sci.* **9**, 143 (1967).
16. O. C. Zienkiewicz, S. Valliapan and I. P. King, Elasto-plastic solutions of engineering problems "initial stress", finite element approach. *Int. J. Num. Meth. Engng* **1**, 75 (1969).
17. J. P. Eimermacher, I. C. Wang and M. L. Brown, Application of the deformation theory of plasticity for determining elastoplastic stress and strain concentration factors. *J. Engng Ind.* **96**, 1152 (1976).
18. A. Needleman, Void growth in an elastic–plastic medium. *J. Appl. Mech.* **39**, 964 (1972).
19. S. Nemat-Nasser and M. Taya, Numerical studies of void growth in a necked bar. *Int. J. Solids Structures* **16**, 483 (1980).
20. H. Andersson, Analysis of a model for void growth and coalescence ahead of a moving crack tip. *J. Mech. Phys. Solids* **25**, 217 (1977).
21. R. D. Thomson and J. W. Hancock, Stress and strain fields around inclusions in a plastically deforming matrix, *Proc. ICM4*, Stockholm, Sweden, Vol. II, p. 733 (1983).
22. M. A. Burke and W. D. Nix, A numerical analysis of void growth in tension creep. *Int. J. Solids Structures* **15**, 55 (1979).
23. J. Perrot et J. L. Chenot, Calcul par éléments finis de l'évolution d'une inclusion dans une matrice déformée uniformément, *Proc. IUTAM Symp. on Physical Non-linearities in Structural Analysis* (Edited by J. Hult and J. Lemaître), p. 216. Springer, Berlin (1981).
24. R. Hill, New horizons in the mechanics of solids. *J. Mech. Phys. Solids* **5**, 66 (1956).
25. J. Cea, *Optimisation, Théorie et Algorithme*. Dunod, Paris (1971).
26. O. C. Zienkiewicz, *The Finite Element Method in Engineering Science*. McGraw-Hill, New York (1973).
27. O. C. Zienkiewicz and E. Hinton, Reduced integration, function smoothing and non-conformity in finite element analysis (with special reference to thick plates). *J. Franklin Inst.* **302**, 443 (1976).
28. N. Kikuchi, Remarks on 4CST-elements for incompressible materials. *Computer Meth. Appl. Mech. Engng* **37**, 109 (1983).

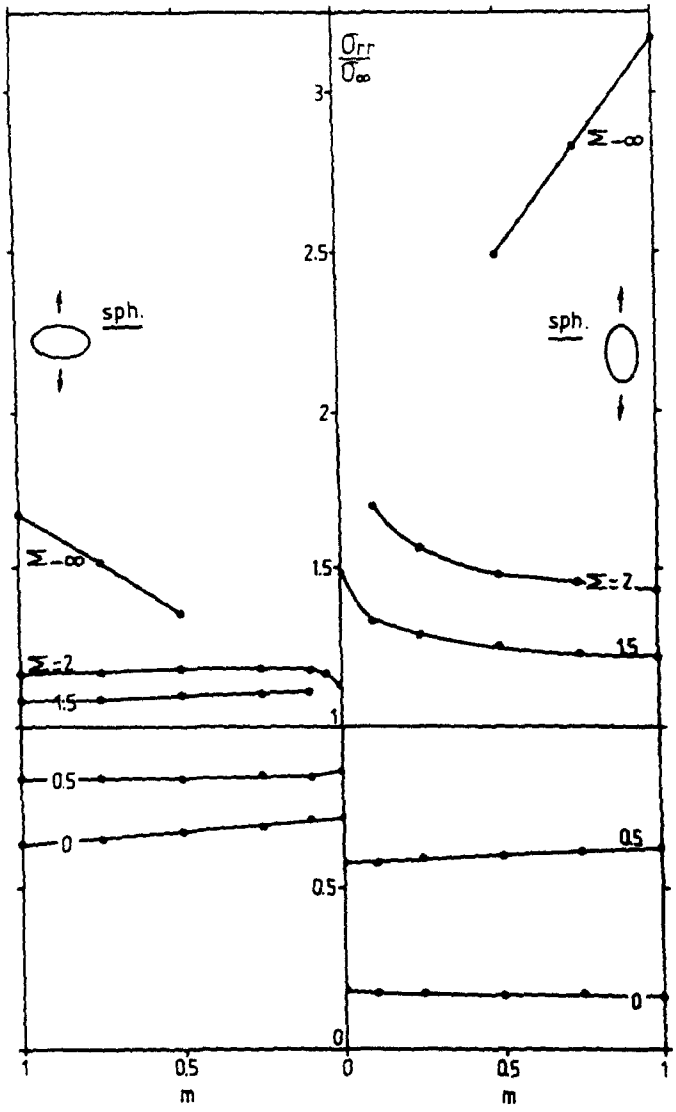

Fig. 15. Same as Fig. 13 for spheroidal inclusions with an aspect ratio equal to 2 (right) or 1/2 (left).

29. G. Duvaut et F. Pistre, Calcul des vecteurs contraintes en approximation P_1 et P_2. *C.r. Acad. Sci. Paris* II **295**, 827 (1982).
30. P. Gilormini et F. Montheillet, Champs de vitesses et de contraintes autour d'une inclusion cylindrique en traction ou compression plane (calcul analytique). *J. Méc. Théorique Appl.* **3**, 563 (1984).
31. B. A. Bilby, J. D. Eshelby and A. K. Kundu, The change in shape of a viscous ellipsoidal region embedded in a slowly deforming matrix having a different viscosity. *Tectonophysics* **28**, 265 (1975).
32. I. C. Howard and P. Brierley, On the finite deformation of an inhomogeneity in a viscous fluid. *Int. J. Engng Sci.* **14**, 1151 (1976).
33. R. D. Thomson and J. W. Hancock, Ductile fracture by void nucleation, growth and coalescence, ME-MM.84.01 Report, Univ. of Glasgow, Scotland (1984).

APPENDIX: ANALYTICAL SOLUTION IN THE CASE OF A LINEARLY VISCOUS MATRIX

The accuracy of the finite element analysis proposed in the present paper was checked by comparing its results with those of the exact analytical solution which is available in the case of an unbounded *linearly* viscous matrix surrounding a single inclusion. A brief description of the analytical solution is given below, where the symmetry axes of the inclusion and the principal axes of the prescribed strain coincide. More details can be found in Refs [11, 30–32].

It is convenient to use a set of elliptical (resp. spheroidal) coordinates r and θ when the inclusion is an

elliptic cylinder (resp. a spheroid) and when the solution in the matrix is needed. These coordinates are defined by

$$x = \left(r - \frac{e}{r}\right)\cos\theta$$
$$y = \left(r + \frac{e}{r}\right)\sin\theta$$

where e depends on the inclusion aspect ratio λ

$$e = \frac{\lambda - 1}{\lambda + 1}.$$

Thus the inclusion corresponds to $r < 1$, the matrix to $r > 1$, and the interface to $r = 1$. The velocity field of the exact solution of the problem is given by

$$\begin{aligned}
u_r^I &= -\frac{\partial kr}{A}\left(1 - \frac{e^2}{r^4}\right)\cos 2\theta \\
u_\theta^I &= \frac{\partial kr}{A}\left(1 + \frac{e^2}{r^4}\right)\sin 2\theta \\
u_r^M &= -\frac{kr}{A}\left[1 + (\delta - 1)\frac{2}{r^2} - \frac{\delta(1 + e^2) - 1}{r^4}\right]\cos 2\theta \\
u_\theta^M &= \frac{kr}{A}\left[1 + \frac{\delta(1 + e^2) - 1}{r^4}\right]\sin 2\theta
\end{aligned} \tag{A1}$$

for plane strain tension or compression (cylindrical inclusion), and

$$\begin{aligned}
u_r^I &= -\frac{\delta kr}{4A}\left(1 - \frac{e^2}{r^4}\right)(3\cos 2\theta - 1) \\
u_\theta^I &= \frac{\delta kr}{4A}\left(3 + 2\frac{e}{r^2} + \frac{e^2}{r^4}\right)\sin 2\theta \\
u_r^M &= -\frac{kr}{4A}\left\{1 - \frac{e^2}{r^4} + \frac{C}{r(r^2 - e)}\left[(1 - e)^2 + \frac{Qr^2}{4e}(3 + 2e + 3e^2)\left(1 - \frac{e}{r^2}\right)^2\right]\right\}(3\cos 2\theta - 1) \\
u_\theta^M &= \frac{kr}{4A}\left\{3 + \frac{2e}{r^2} + \frac{3e^2}{r^4} + \frac{C}{r(r^2 + e)}(3 + 2e + 3e^2)\left[1 + \frac{Qr^2}{4e}\left(3 + \frac{2e}{r^2} + \frac{3e^2}{r^4}\right)\right]\right\}\sin 2\theta
\end{aligned} \tag{A2}$$

for axially symmetric tension or compression (spheroidal inclusion). In the above equations superscripts I and M refer to the inclusion and the matrix, respectively, δ was defined in the text

$$A = (1 + e^2/r^4 + 2e/r^2\cos 2\theta)^{1/2}$$
$$Q = 1 - \frac{r^2 + e}{2r\sqrt{e}}\tanh^{-1}\left(\frac{2r\sqrt{e}}{r^2 + e}\right) \qquad \text{for } \lambda > 1 \text{ (prolate spheroid)}$$
$$Q = 1 - \frac{r^2 + e}{2r\sqrt{-e}}\tan^{-1}\left(\frac{2r\sqrt{-e}}{r^2 + e}\right) \qquad \text{for } \lambda < 1 \text{ (oblate spheroid)}$$
$$C = \frac{(\delta - 1)(1 + e)}{1 + Q_1\dfrac{3 + 2e + 3e^2}{4e}}$$

and Q_1 is the value taken by Q for $r = 1$.

Equations (A1) and (A2) define incompressible velocity fields which are continuous across the interface and correspond to a homogeneous deformation within the inclusion. It can be checked that these equations give the exact solution of the problem by (a) deriving the associated strain rate components, (b) applying the flow rule (eqn (5)) in the matrix and the inclusion, and (c) eventually solving the equilibrium equation which gives the hydrostatic pressure in the inclusion (eqns (26)) and in the matrix

$$\begin{aligned}
p_M &= p_\infty - \frac{4}{3}k\sigma_M\frac{\delta - 1}{r^2A^2}\left(\cos 2\theta - \frac{e}{r^2}\right) \\
p_M &= p_\infty - \frac{2}{3}k\sigma_M\frac{C}{r}\left[\frac{r^2 + e}{r^2A^2} + \frac{r^2}{r^2 + e}(Q - 1)\right]
\end{aligned} \tag{A3}$$

in the plane strain and axially symmetric cases, respectively.

It can moreover be shown that the last condition to be fulfilled, i.e. the continuity of stress tension across the interface, requires δ to be given by eqns (25). Appropriate formulae for the gradient and divergence operators in the case of curvilinear coordinates are of course to be used all along the calculations.

During the tests of the finite element analysis described in this paper, eqns (A1) and (A2) were applied to prescribe the velocity field at the mesh boundaries, eqns (A3) and the equivalent strain rate associated with eqns (A1) and (A2) were used to obtain the full curves in Figs 2–4(c) and (d), 5(b)–(d) and 6(a) and (b).